

# Towards understanding the superfluid behavior in double layer graphene nanostructures

Brian Dellabetta · Matthew J. Gilbert

Published online: 29 May 2013  
© Springer Science+Business Media New York 2013

**Abstract** The unique electronic properties that are found in graphene layers have been touted as an attractive means to not only study fundamental physical principles but to design new types of electronic and optical information processing technologies. Of the physical observables present in graphene which may be exploited for device technologies, the proposed superfluid phase transition of indirectly bound excitons in closely spaced layers of graphene is one of the most exciting. Nevertheless, the superfluid phase of double layer graphene remains a poorly understood quantity. In this work, we theoretically investigate the properties of the superfluid phase in double layer graphene systems via two disparate methods: path-integral quantum Monte Carlo and non-equilibrium Green's functions. We show that the superfluid phase in double layer graphene persists up to ambient temperatures in spinless systems. When we increase the number of degrees of freedom in the system to include spin, we find that the screening effectiveness is suppressed by intralayer correlations resulting in higher transition temperatures than previously predicted. Furthermore, we estimate the magnitude of the interlayer currents that the superfluid can sustain under non-ideal conditions by considering the effects of layer disorder and the electron-phonon interaction. We show that the superfluid dynamics is significantly affected not only by the total amount of disorder

but also depends very heavily on the location of the disorder in the layers. When the electron-phonon interaction is included, we demonstrate that for high layer carrier densities the electron-phonon interaction does not affect superfluid flow but degrades the transport properties significantly as the layer carrier concentration decreases.

**Keywords** Graphene · Excitonic condensation · Superfluidity · NEGF · Path integral · Quantum Monte Carlo

## 1 Introduction

Dipolar excitons, composite bosons comprised of fermionic electron and hole quasiparticle pairs bound together via an attractive Coulomb interaction, are of particular interest both from a standpoint of fundamental physics and potential device application. As excitons involve short range Coulomb attractions to mediate the superfluid phase transition rather than the typical long range electron-phonon interactions responsible for s-wave superconductivity, the binding energy has the potential to be significantly larger and may allow superfluidity to persist to much higher temperatures. Nevertheless, the experimental observation of excitonic superfluidity in bulk semiconductors is fundamentally limited by the short lifetimes of directly bound excitons [1]. While for many years this lack of sufficient excitonic lifetimes has been the limiting factor in the realization of excitonic superfluidity, this limitation can be overcome through the use of indirectly bound excitons in which electrons and holes are spatially segregated yet still interact via a Coulomb attraction to form excitonic quasiparticles. To this end, dipolar excitonic superfluidity mediated by the condensation of indirectly bound

---

This work was supported by the Army Research Office under Contract No. W911NF-09-1-0347.

B. Dellabetta (✉) · M.J. Gilbert  
Department of Electrical and Computer Engineering, University of Illinois, Urbana, IL 61801, USA  
e-mail: [dellabel@illinois.edu](mailto:dellabel@illinois.edu)

M.J. Gilbert  
e-mail: [matthewg@illinois.edu](mailto:matthewg@illinois.edu)

excitons has appeared in a diverse set of systems such as microcavities [2–4] and cold atom systems [5–9].

Beyond these condensed matter systems, coupled semiconductor quantum wells have provided a rich solid state playground within which to observe dipolar excitonic superfluidity. The search for dipolar excitonic superfluidity in coupled quantum well systems has found significant experimental [10–21] and theoretical progress [22–35] in the Quantum Hall regime. In this operational regime, each layer has a filling factor of  $\nu_{\text{layer}} = \frac{1}{2}$  for a total filling factor of  $\nu_{\text{total}} = 1$ . At this filling factor, there are equivalent concentrations of electrons and hole quasiparticles in each layer with equivalent dispersion relations, so that electrons in one layer indirectly bind with holes in the other layer across a thin dielectric barrier via an interlayer Coulomb interaction.

While superfluids in quantum Hall bilayers are physically interesting systems, they are technologically impractical due to the large magnetic fields and low temperatures that the Quantum Hall regime requires. There has been an intense interest in replacing the quantum wells with graphene monolayers separated by a thin tunnel dielectric as this system has been predicted to yield far more robust excitonic superfluid states [36–38]. Graphene [39] possesses many attributes that make it an ideal alternative to quantum wells within which to observe dipolar exciton superfluidity, as it is an atomically thin two-dimensional Dirac semimetal with a symmetric dispersion relation for both electrons and holes, can sustain high carrier concentrations, and is expected to be a poor at screening additional charges, due to its two-dimensional nature. These properties combine to provide the possibility of finding a superfluid in double layer graphene above cryogenic temperatures and without the presence of a magnetic field to quench the kinetic energy of the system.

The possibility of finding an excitonic superfluid outside of the forbidding quantum Hall region is quite an exciting prospect in and of itself, but this system has also been predicted to be of significant technological relevance as a post-CMOS (Complementary Metal Oxide Semiconductor) logic device. The vast majority of information processing performed today is done via a MOSFETs (Metal Oxide Semiconductor Field Effect Transistors). Current MOSFET technology is based on a set of independently moving electrons. A particularly attractive way to enable next-generation logic devices is by harnessing the collective motion of quasiparticles. In this case, switching from an “on” state to an “off” state can, in principle, be performed using smaller voltages without loss in other relevant device characteristics [40–42]. Therefore, in addition to understanding the basic physical properties of the superfluid phase, we wish to theoretically explore the design space necessary for optimizing the design of this system for potential device implementation.

In this invited contribution, we use fermionic path-integral quantum Monte Carlo (PIMC) and non-equilibrium

Green’s function (NEGF) methods to study the properties of excitonic superfluids in double layer graphene under a variety of conditions. We begin in Sect. 2 by fully describing the system we study, as well as the general parameters for the dimensions and materials properties of our system. In Sect. 3, we begin to classify the equilibrium response of the expected superfluid phase transition using the PIMC formalism. First we calculate the Kosterlitz-Thouless transition temperature ( $T_{KT}$ ) for a spinless system of fermions. We present additional insight into the nature of this transition from the examination of the corresponding two-body correlation functions both above and below  $T_{KT}$ . We then expand our analysis to determine how  $T_{KT}$  changes when additional fermionic degrees of freedom (e.g. spin) are considered. In Sect. 4, we move beyond the equilibrium response of the double layer graphene nanosystem to discuss the non-equilibrium response. Here we define a mean-field approximation to the interacting Hamiltonian and then apply the NEGF quantum transport formalism to compare the ideal transport characteristics of the double layer graphene system with disordered systems and those in which the electron-phonon interaction is considered. We find that with careful control over the design of the double layer graphene system that the effects of disorder and the electron-phonon interaction may be mitigated thereby allowing the superfluid phase to persist in the presence of these interactions.

## 2 Device description

In Fig. 1, we show a schematic of the theoretical system of interest in this work. Here, we consider two zigzag graphene nanoribbon monolayers assumed to be perfectly aligned with one another and separated by a 1 nm thick  $\text{SiO}_2$  tunnel dielectric. Contacts are placed along the edges of top left

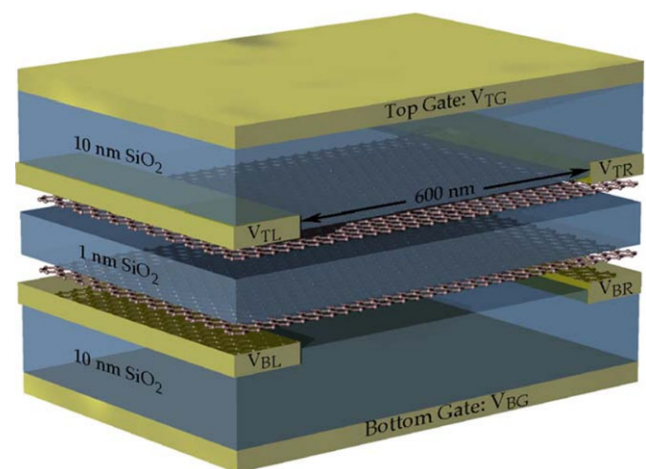


**Fig. 1** Schematic depiction of the double layer graphene system under consideration in this work. Adapted from [38]

( $V_{TL}$ ), top right ( $V_{TR}$ ), bottom left ( $V_{BL}$ ) and bottom right ( $V_{BR}$ ) to inject and extract current. We use top ( $V_{TG}$ ) and bottom gates ( $V_{BG}$ ) to manipulate the quasiparticle concentrations in each of the layers thereby populating one with electrons and the other layer with holes. Each of these gate contacts is separated from the graphene system by 10 nm thick regions of  $\text{SiO}_2$ . We consider each of the oxide regions to be perfect in the sense that they do not contain any stray charges and have perfect interfaces with the graphene layers. In terms of notation, we choose the  $\hat{x}$  direction to lie along the length of the system, the  $\hat{y}$  direction to lie along the width and the  $\hat{z}$  along the depth.

### 3 Classifying the equilibrium response

The superfluid phase transition we study is inherently a many-body effect, thereby making it impossible to study with standard device simulations. This necessitates the use of inherently many-body techniques such as PIMC as opposed to single particle methods in which many-body effects are introduced via a mean-field approximation. PIMC methods, which have previously been used in fermionic [43] and electronic [44] systems, can directly simulate such a strongly correlated system, and are thus ideal for yielding insight into the critical system parameters needed to quantify the properties of the superfluid state.

We begin by realizing that in the path-integral formalism of quantum statistical mechanics, the many-body thermal density matrix is represented by a sum over imaginary time paths [45],

$$\begin{aligned} \rho(R, R'; \beta) &\equiv \frac{1}{Z} \sum_i \Psi_i(R) \Psi_i^*(R') e^{-\beta E_i} \\ &= \frac{1}{Z} \int_{R(0)=R'}^{R(\beta\hbar)=R} \mathcal{D}R(\tau) e^{-\frac{1}{\hbar} S_E[R(\tau)]}, \end{aligned} \quad (1)$$

which involves a path integral over the position coordinates of all quantum particles.  $\Psi_i(R)$  is a many-body eigenstate of the Hamiltonian, which we discuss below, with energy  $E_i$ .  $\beta = 1/k_B T$  is the inverse temperature and the partition function  $Z$  normalizes the density matrix  $\rho$ . The integral represents a sum over random walks  $R(\tau)$  taking place in “imaginary time”  $\tau$ , beginning at ( $R'$ ,  $\tau = 0$ ) and ending at ( $R$ ,  $\tau = \beta\hbar$ ). Each path is weighted by the real-valued Euclidean action, defined by the functional

$$S_E[R(\tau)] = \int_0^{\beta\hbar} \left[ \frac{m}{2} |\dot{R}|^2 + V(R(\tau)) \right] d\tau, \quad (2)$$

which involves a sum of the kinetic energy and the potential energy,  $V(R(\tau))$ , arising from the repulsive intralayer and attractive interlayer Coulomb interactions. The path integral becomes a sum over closed paths, tracing over paths

$R = R'$  to compute expectation values for quantities of interest. Particles thus appear within the path integral context as closed loops roughly the size of the de Broglie wavelength,  $\lambda_{dB} = h/\sqrt{2\pi m k_B T}$ . For identical particles, an additional sum over permutations is necessary,

$$\begin{aligned} \rho(R, R'; \beta) &= \frac{1}{Z} \frac{1}{N!} \sum_P (\pm 1)^P \\ &\times \int_{R(0)=R'}^{R(\beta\hbar)=PR} \mathcal{D}R(\tau) e^{-\frac{1}{\hbar} S_E[R(\tau)]}, \end{aligned} \quad (3)$$

so that the many-body wave function has the appropriate  $(\pm 1)^P$  symmetrization or anti-symmetrization whereby the many-body wave function acquires a minus sign under exchange for fermionic systems. If  $\lambda_{dB}$  is much less than interparticle spacing, the identity permutation dominates the sum, but a large  $\lambda_{dB}$ , normally found at low temperatures, contains significant contributions from all  $N!$  permutations. The introduction of permutations leads to a percolation transition for bosons, in which large chains of bosons span the sample. This is identified with the superfluid phase transition [46].

The  $(-1)^P$  term yields what is commonly referred to as the fermion sign-problem that results in exponential inefficiencies in quantum Monte Carlo simulations. This issue is handled with a ground-state fixed node approximation [47]. The fixed-node approximation maps the fermionic density matrix onto an effective bosonic density matrix that is easily solved with PIMC. This approach has been previously used in paired fermionic system [48, 49] and electron-hole condensates [50, 51] to compute relevant system observables. In this work, at every slice on the path, the electron and hole coordinates are placed into a Slater determinant,

$$\det |\phi(\mathbf{r}_{e,i} - \mathbf{r}_{h,j})|, \quad (4)$$

which incorporates an s-wave pairing wave function  $\phi(r) = e^{-r/a}$  based on an excitonic wave function. The exciton pairing radius, or coherence length, is set to  $a = 2.3$  nm but results are largely insensitive to the parameter for  $a = 1$ –10 nm. All paths that cross nodes of this wave function are rejected in sampling to exclude from the path integral all paths which change the sign of the Slater determinant. The selection rule effectively eliminates all negative terms to give an approximate solution to the fermionic path integral. As the fixed-node approximation is exact in only one dimensional systems, there will be fixed-node “errors” introduced into the simulations mainly arising from the poor correspondence of nodes in the trial density matrix with those of the actual system [52]. In the double layer graphene system, we may minimize these errors by studying a symmetric system with a very simple nodal structure consisting of free particle nodes in both spatial dimensions and a well-known BCS

pairing function representing the presumed s-wave pairing in the superfluid.

Interacting particles in a condensate seek to occupy the same single-particle ground state, but there is a competing repulsion as they try to reduce potential energy. The competition yields a many-body state that can be described by the condensate fraction or the superfluid density. To calculate this value, we first construct the single-particle density matrix,

$$\rho_1(\mathbf{r}, \mathbf{r}') = \langle \psi_T^\dagger(\mathbf{r}) \psi_B(\mathbf{r}) \psi_T(\mathbf{r}') \psi_B^\dagger(\mathbf{r}') \rangle, \tag{5}$$

where angle brackets indicate a thermal average expectation value over the many-body wave function. In general, the single particle density matrix involves 2 field operators. In this system, however, each boson consists of a composite exciton comprised of one electron and one hole quasiparticle. The single-particle density matrix is thus comprised of four fermionic field operators, totaling 2 bosonic field operators. A large occupation of a single state is a manifestation of the condensate phase, with condensate fraction equivalent to the occupation expectation value.

The graphene quasiparticle Hamiltonian, which has the form of a Dirac Hamiltonian [39],

$$H_{Dirac} = (-i\hbar v_F \boldsymbol{\alpha} \cdot \nabla), \tag{6}$$

is not amenable to PIMC methods due to the linear wave vector dependence. Each monolayer is instead modeled as a parabolic semiconductor with identical electron and hole mass. The Hamiltonian in this case is [51]

$$H_{eh} = \sum_{i=1}^{N_e} \frac{p_{i,e}^2}{2m^*} + \sum_{i=1}^{N_h} \frac{p_{i,h}^2}{2m^*} + \sum_{i < j} \frac{e^2}{\epsilon |\mathbf{r}_{i,e} - \mathbf{r}_{j,e}|} + \sum_{i < j} \frac{e^2}{\epsilon |\mathbf{r}_{i,h} - \mathbf{r}_{j,h}|} - \sum_{i,j} \frac{e^2}{\epsilon \sqrt{|\mathbf{r}_{i,e} - \mathbf{r}_{j,h}| + d^2}}, \tag{7}$$

which accounts for the electron and hole quasiparticle kinetic energy, the electron and hole intralayer repulsion, and the interlayer attraction, respectively. We set  $\epsilon = 3.9\epsilon_0$  to correspond to the SiO<sub>2</sub> barrier dielectric while allowing the layer separation length  $d$  to be a degree of freedom we may vary. To set the effective mass, and restore the connection with graphene, we require that the Fermi velocity match the quasiparticle velocity of graphene,  $v_F = 10^6$  m/s [53]. For a quasiparticle density  $n$ , this condition yields

$$m^* = \hbar \sqrt{\frac{4\pi n}{g v_F^2}}, \tag{8}$$

where  $g$  is the degeneracy due to spin and valley degrees of freedom. Unless specified otherwise, electron and hole

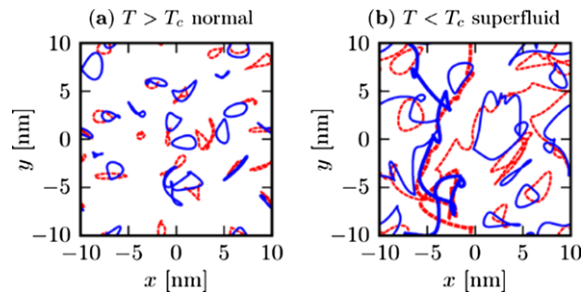


**Fig. 2** Typical paths of electron (solid blue) and hole (dashed red) quasiparticles for graphene monolayers separated by  $d = 0.5$  nm, with excitons emerging as nearby electron and hole paths. **(a)** Above  $T_{KT}$ , particle paths are localized by thermal wavelength  $\lambda_{dB}$ , indicating the absence of a superfluid. **(b)** Below  $T_{KT}$ , a condensate emerges, as revealed by long permuting chains (shown by thicker lines) that wrap around the periodic simulation cell. Adapted from [38]

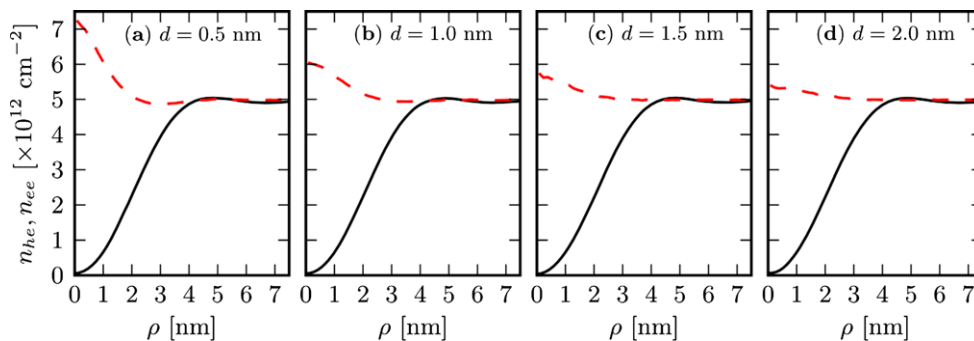
concentrations are set to  $n_e = n_h = 5 \times 10^{12}$  cm<sup>-2</sup>, which is a value of quasiparticle density close to the maximum value [39]. Using these parameters, Eq. (8) yields an effective mass of  $m^* = 0.09 m_e$ .

As we work in the canonical ensemble, we are unable to include electron-hole recombination, so single-particle tunneling between layers can not be explicitly included within our PIMC framework. However, single-particle tunneling amplitude is expected to be small in the system and neglecting recombination should not qualitatively change the results. Instead, the Coulomb tunneling enhancement in the model must be inferred from analysis of interlayer electron-hole correlations.

With the foundations for the application of PIMC exploring the superfluid aspects of a double layer graphene system, we begin with the simplest case of spinless quasiparticles. Figure 2 depicts the path permutations calculated in the PIMC formalism for a double layer graphene-like system with interlayer spacing  $d = 0.5$  nm. The periodic simulation square is 20 nm in both the length and width while each layer contains 20 quasiparticles each resulting in the aforementioned layer electron and hole density of  $n_e = n_h = n = 5 \times 10^{12}$  cm<sup>-2</sup>. The exciton paths at  $T = 1200$  K, shown in Fig. 2(a), are localized on the order of  $\lambda_{dB}$ , indicating that we have not crossed the superfluid phase boundary. However, we can clearly see that the electrons and holes are sitting in very close proximity to one another above the superfluid transition temperature thereby indicating that the electrons and holes are still paired as preformed excitons which have not condensed. This is to be contrasted with Fig. 2(b) where we show that when the temperature is reduced to  $T = 300$  K, the paths now form long permuting chains that wind around the simulation cell, indicating the long range order expected with excitonic superfluidity.

To gain additional information on the exciton formation and interlayer correlations, we examine at the pair correla-

**Fig. 3** Room temperature electron-hole (red dashed) and electron-electron (black solid) correlation functions for interlayer separations of 0.5, 1.0, 1.5, and 2.0 nm, respectively. Adapted from [38] (Color figure online)



tion function,

$$n_{he}(|\mathbf{r} - \mathbf{r}_0|) = \frac{\langle n_h(\mathbf{r})n_e(\mathbf{r}_0) \rangle}{\langle n_e(\mathbf{r}_0) \rangle}, \tag{9}$$

that calculates the average density of holes at point  $\mathbf{r}$  in one graphene monolayer given an electron at point  $\mathbf{r}_0$  in the other monolayer.  $n_e(\mathbf{r})$  and  $n_h(\mathbf{r})$  are the quantum mechanical density operators,  $n_e(\mathbf{r}) = a^\dagger(\mathbf{r})a(\mathbf{r})$ . Intralayer correlation functions  $n_{ee}$  and  $n_{hh}$  can likewise be defined to quantify the degree of repulsion from equal-charge quasiparticles. We plot the correlation functions in Fig. 3 as the interlayer separation is increased. Evidence of the formation of excitons is seen by a maximum (minimum) in  $n_{he}$  ( $n_{ee}$ ) that begins to decay as interlayer separation increases. Electron-hole correlation is essentially independent of interlayer separation for  $d > 2.0$  nm, necessitating that the layers be within 1.0 nm of one another in order for condensation to occur [38].

### 3.1 Screening of additional fermion flavors

One of the most significant outstanding questions in the behavior of superfluids in double layer graphene is the location of  $T_{KT}$ . There has been a very active debate in the literature as to the impact of screening on the strength of the interlayer Coulomb interaction required to drive the superfluid phase transition. In order to answer this question, one must elucidate the role of screening on the transition temperature. In the works that predict a high transition temperature [36–38], the fermionic degrees of freedom were assumed to be constrained by the large energy gap of the system resulting from the binding of the interlayer quasiparticles into a condensate. This assumes that the quasiparticles lose their individual fermionic character when they form an exciton and are no longer able to screen the interlayer interactions that drive the superfluid transition. Nevertheless, other work on the double layer graphene system indicate that each of the additional individual fermionic degrees of freedom add to effectively screen out the interlayer interaction leading to a sharp reduction in the transition temperature [54]. In our analysis thus far we have only considered two fermion flavors in the system ( $N_f = 2$ ) where the quasiparticles have a

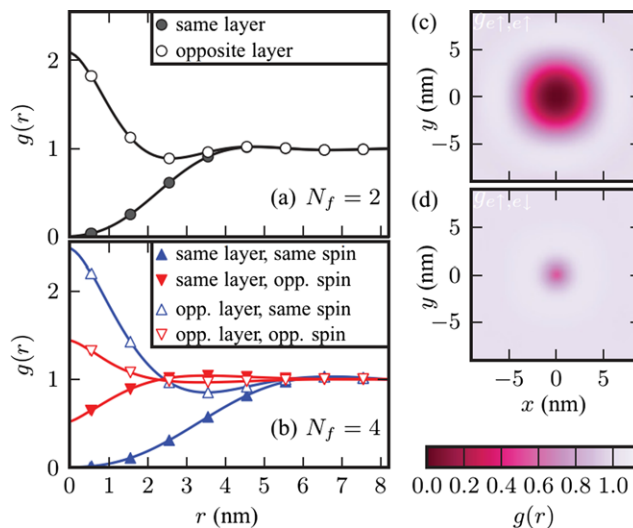


**Fig. 4** Pair correlation functions for the (a) spinless and (b) spin- $\frac{1}{2}$  systems. Intralayer exchange correlation functions for (c) equal spin species,  $g^{\uparrow\uparrow}(\mathbf{r}_{ij})$  and (d) opposite spin species,  $g^{\uparrow\downarrow}(\mathbf{r}_{ij})$ . Adapted from [55]

“which layer” degree of freedom. To shed light on this important issue, we now extend the spinless model to account for both layer and spin degrees of freedom ( $N_f = 4$ ). The quasiparticle Hamiltonian does not change from the form set in Eq. (7); the spin only enters into the calculation when considering fermion antisymmetry under interchange.

To further understand the effects of increased fermion flavor and screening, we return to the real-space correlation function among the quasiparticles, Eq. (9) for the spinless and spin- $\frac{1}{2}$  systems cases at  $T = 150$  K with an interlayer separation of  $d = 0.5$  nm using 10 spin up and 10 spin down particles in each layer. In Fig. 4(a), we plot the pair correlation functions for the spinless ( $N_f = 2$ ) case where we use an electron in the bottom layer as the test particle and record the positions of the other corresponding quasiparticles in both the top and bottom layer. We observe that an exchange hole forms around the test particle, as is expected for identical fermions. Additionally, we find an accumulation of holes sitting directly on top of the electron in the opposite layer signaling the formation of indirectly bound excitons.

This is to be contrasted with Fig. 4(b) where we now observe that the exchange hole has increased in size, but this can be explained simply as the number of quasiparticles of a particular flavor has now decreased. We still observe the signs of an indirect condensate that we observed in the spinless case, where holes sit directly on top the electrons, but now we also see the effects of the additional degrees of freedom emerge. We see that the quasiparticles in the same layer with opposite spin are not screened by the Coulomb interaction, as Pauli exclusion exerts no repulsive effect. This leads to a significant number of fermions sitting close to the position of the test particle effectively weakening the interlayer Coulomb interaction that drives the phase transition. Furthermore, this also implies that when the quasiparticles pair into the bosonic excitons then individual constituent particles retain their fermionic identity. When we plot the pair correlation functions in two dimensions, then this behavior becomes quite clear. In Fig. 4(c), we again show the pair correlation function for the spinless quasiparticles to highlight the intralayer interactions. Once again, the exchange hole between identical fermions is prominently displayed with no spin to highlight this marked decrease in intralayer repulsion when spin is considered. Meanwhile in Fig. 4(d), for the  $N_f = 4$  case, we observe a much smaller correlation hole as particles with opposite spin may sit close to the test particle as a result of Pauli exclusion.

### 3.2 Superfluid transition temperature in double layer graphene

Beyond PIMC giving us access to the correlation functions, we wish to take advantage of the fact that PIMC gives us access to the full thermal density matrix to estimate the value of  $T_{KT}$ . We do so by calculating the temperature dependence of the superfluid fraction ( $\rho_s/\rho$ ), or the ratio of excitons in the condensate phase relative to the total number of excitons present in the system. The superfluid fraction is a meaningful number to examine to determine  $T_{KT}$  as it saturates at unity when the system is fully condensed and tends to zero above the transition temperature. The superfluid fraction is related to the topological winding number [56],

$$\frac{\rho_s}{\rho} = \frac{mk_B T}{\hbar^2(N_e + N_h)}(W_x^2 + W_y^2), \tag{10}$$

where  $W_x$  and  $W_y$  are the topological winding numbers of the constituent quasiparticles. Within PIMC these are collected by tracking the number of times that a path winds around the periodic solution domain in both spatial directions. Tightly paired excitons in the condensed regime yield large, even winding numbers as they form long permuting chains that wrap around the simulation cell in pairs. When no condensation occurs, there would be no winding about

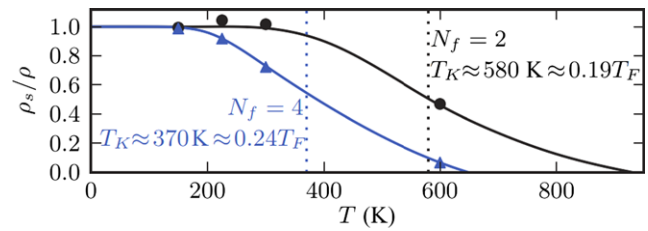


**Fig. 5** Dependence of superfluid fraction  $\rho_s/\rho$  on temperature for the spinless (black circles) and spin- $\frac{1}{2}$  (blue triangles) quasiparticle models for an interlayer separation of  $d = 0.5$  nm. The vertical dashed lines denote the transition temperature, the temperature at which superfluid fraction reaches one half. Adapted from [55] (Color figure online)

the simulation region and we expect to see a peak in the winding numbers at only the trivial value,  $W_x = W_y = 0$ .

In Fig. 5, we show the calculated superfluid fraction as a function of the system temperature for both the spinless and spin- $\frac{1}{2}$  scenarios. We find that the insight provided by the pair correlation function of a weakened Coulomb interaction resulting from the increased fermion flavor results in a suppressed transition temperature, with a drop from  $T_{KT} \approx 580$  K in the spinless case to  $T_{KT} \approx 370$  K in the spin- $\frac{1}{2}$  case indicating that the additional degrees of freedom weaken the interlayer Coulomb interaction. The observed drop in transition temperature may even, in fact, be expected from reduced quantum degeneracy without accounting for screening. An ideal Bose gas has a transition temperature  $T_{KT} \sim (n\lambda_{dB})^{-1/2}$ , where  $n$  is the density of identical bosons. Adding more degenerate flavors decreases the density  $n$  by  $1/N_f$ , resulting in a suppressed transition temperature. The transition temperature scales relatively closely with Fermi temperature, shifting from  $T_{KT} \approx 0.19T_F$  to  $T_{KT} \approx 0.24T_F$  when spin is added, once again indicating increased fermion flavors are not completely screened by the condensate. Therefore, while the large- $N$  calculation finds enhanced screening with increasing fermion flavors [54], our work suggests a weaker trend [55]. The reason for this difference is excitonic binding and correlation between different fermion flavors. In the large- $N$  expansion, the starting point is RPA-like screening. Because each flavor can screen independently, the system exhibits weak BCS pairing of states near the Fermi surface when the temperature is below  $T_{KT}$ . In our simulations, we have strong excitonic pairing which organizes the quasiparticles into neutral excitons and suppresses their ability to screen. This excitonic pairing and correlation between quasiparticles of different spin is not present in the large- $N$  approximation’s perturbative expansion.

### 4 Classifying the non-equilibrium response

With an understanding of the equilibrium system response, we now seek to understand the non-equilibrium response.

While PIMC provides strong insights into the equilibrium response, the method is not capable of studying the response far from equilibrium, namely the observables expected in quantum transport studies. The non-equilibrium Green's function (NEGF) method is a useful tool for estimating the experimentally observable transport in the system [57]. In the NEGF study, we set each monolayer to be 30 nm long by 10 nm wide, and are separated by dielectric 1 nm thick. The top and bottom gates ( $V_{TG} = -V_{BG}$ ) are set to yield individual carrier concentrations of  $10^{13} \text{ cm}^{-2}$  in each layer, which correspond to a Fermi energy in the top (bottom) layer of 0.4 eV ( $-0.4 \text{ eV}$ ). The gate bias conditions and the interlayer separation have been chosen to be consistent with the requirements for room temperature condensation predicted in the PIMC simulations [38] as well as many-body theory [36, 37]. In practice, this is a non-trivial density to achieve due to the large electric fields required. However, in our system we calculate the electric field required to achieve these carrier concentrations to be  $8 \times 10^6 \text{ V/cm}$  between the top and bottom monolayers. While this value is large, it is below the dielectric breakdown voltage for  $\text{SiO}_2$ .

We wish to capture the salient physics of the double-layer graphene system within a mean-field representation of the interactions. We begin by defining the Hamiltonian [57, 58] in the atomistic tight-binding description for an individual graphene monolayer,

$$H_{TL} = \sum_{(i,j)} -t|i\rangle\langle j| + V_i|i\rangle\langle i|, \quad (11)$$

where lattice points  $i$  and  $j$  are first nearest neighbors.  $t = 3.0 \text{ eV}$  is the nearest neighbor hopping energy for the  $p_z$  orbital of graphene, which allows for the unique low-energy linear dispersion at the  $K$  and  $K'$  points in the Brillouin zone. Nearest neighbor  $p_z$  orbital hopping is the predominant interaction for graphene in the probed energy range, and longer range hopping is neglected. The electrostatic interactions are included in the on-site potential energy term,  $V_i = \phi(\mathbf{r}_i)$ , that is calculated via a 3-dimensional Poisson solver. We must also make a choice as to the type of model we use to implement the contacts to our double layer graphene system. In this work, we use a phenomenological model to simulate a generic metal contact with a constant density of states [59, 60]. This model captures the basic self-energy needed to appropriately simulate a metal contact without taking into account multiple orbitals or complex interface problems such as lattice mismatch or Schottky barrier height.

We expand the single-layer Hamiltonian to the double layer Hamiltonian by coupling the top and bottom monolayers using the following Bogoliubov-de Gennes (BdG) Hamiltonian,

$$\mathcal{H}_{BdG} = \begin{bmatrix} H_{TL} & 0 \\ 0 & H_{BL} \end{bmatrix} + \sum_{\mu=x,y,z} \hat{\mu} \cdot \mathbf{\Delta} \otimes \sigma_{\mu}, \quad (12)$$

where the mean-field interlayer interaction includes both a single particle tunneling and many-body contribution,  $\mathbf{\Delta}$ . In Eq. (12),  $\mu$  represents a vector that isolates each of the three Cartesian components of the pairing vector,  $\sigma_{\mu}$  represents the Pauli spin matrices in each of the three spatial directions, and  $\otimes$  represents the Kronecker product. In general, the single-particle Hamiltonian for the hole layer is the same as Eq. (11), but the sign is flipped to take hole quasiparticles into account,  $H_{BL} = -H_{TL}$ . In the scope of graphene, however, the Hamiltonian is particle-hole symmetric and the system is not affected by this change.

With the basic system Hamiltonian defined, we now examine the many-body interlayer interaction in the Hamiltonian. Within the Hartree-Fock mean-field approximation, the model to account for interlayer exchange is

$$H_{int} = \sum_{\lambda} \langle i', \alpha' | V_{mf} | \alpha, i \rangle, \quad (13)$$

where  $i$  represents the layer degree of freedom and the sum is over all eigenstates  $\lambda$  of the system. In real space, this simplifies to

$$H_{int} = -U\rho(r_i, r_j), \quad (14)$$

where the strength of the interlayer interaction is characterized by the on-site Coulomb term,  $U$ , whose selected value we address below. We assume that the graphene monolayers are perfectly registered, and approximate the pairing in the mean-field picture such that electrons at site  $r_i$  in the top layer only bind with holes at site  $r_j$  on the bottom layer when  $i = j$ . We thus neglect inter-sublattice exchange interactions in the NEGF studies, as self-consistent computations of this magnitude quickly become intractable. In this work, we simplify the understanding of the dynamics through the use of the pseudospin language where the *which layer* degree of freedom is represented as a spin- $\frac{1}{2}$  fermion; the top (bottom) layer is replaced by the  $|\uparrow\rangle$  ( $|\downarrow\rangle$ ) pseudospin state. The density matrix  $\rho$  in the pseudospin language is

$$\rho = \begin{bmatrix} \rho_{\uparrow\uparrow} & \rho_{\uparrow\downarrow} \\ \rho_{\downarrow\uparrow} & \rho_{\downarrow\downarrow} \end{bmatrix}. \quad (15)$$

The on-diagonal components of the density matrix ( $\rho_{\uparrow\uparrow}$ ,  $\rho_{\downarrow\downarrow}$ ) correspond to the associated electron and hole densities of the top and bottom monolayers, respectively. The off-diagonal components determine the interlayer interactions, as seen in Eq. (14).

The order parameter resulting from the spontaneous symmetry breaking in the superfluid phase,  $m_{exc}$ , involves coupling between  $|\uparrow\rangle$  and  $|\downarrow\rangle$  pseudospin states. It is thus proportional to the off-diagonal terms of the density matrix [58, 61],

$$\begin{aligned} m_{exc}^x &= \rho_{\uparrow\downarrow} + \rho_{\downarrow\uparrow} = 2\text{Re}(\rho_{\uparrow\downarrow}), \\ m_{exc}^y &= -i\rho_{\uparrow\downarrow} + i\rho_{\downarrow\uparrow} = 2\text{Im}(\rho_{\uparrow\downarrow}). \end{aligned} \quad (16)$$

The single particle density matrix is directly calculated within the NEGF formalism. The solution procedure is to iterate over the above mean-field equations to calculate the single particle density matrix from which we obtain the interactions and the carrier densities. The carrier densities are then input quantities to the Poisson equation for electrostatics from which an electrostatic potential is calculated. The electrostatic potential is then fed back into the NEGF formalism to obtain a self-consistent solution with compatible particle densities and potential profile, utilizing the Broyden method [62] to accelerate convergence.

Yet before proceeding further in our analysis of the quasi-particle transport dynamics, we must gain a clearer understanding of the interlayer interactions. To do so, we rewrite Eq. (12) in a more simplified form in which interlayer interactions are expressed in terms of directional pseudospin components [63],

$$\mathcal{H}_{BdG} = \begin{bmatrix} H_{TL} + \Delta_z & \Delta_x - i\Delta_y \\ \Delta_x + i\Delta_y & H_{BL} - \Delta_z \end{bmatrix}. \tag{17}$$

The directional components of the interlayer interactions  $\Delta$  are expressed as

$$\begin{aligned} \Delta_x &= (\Delta_{sas} + Um_{exc}^x) \\ \Delta_y &= Um_{exc}^y \\ \Delta_z &= \frac{1}{2}(V_{\uparrow} |i\rangle\langle i| - V_{\downarrow} |i\rangle\langle i|). \end{aligned} \tag{18}$$

The on-diagonal term in the interlayer interactions,  $\Delta_z$ , corresponds to a term in the Hamiltonian that is much like a Zeeman field splitting term, and it acts to decrease the order parameter by separating the two Fermi surfaces. The single particle tunneling energy,  $\Delta_{sas}$ , is proportional to the probability of a single electron tunneling event through the thin dielectric and recombining with a hole. As single-particle tunneling is an adverse event, it is desirable to have a very thick barrier in between the two graphene layers to maximize the lifetime of the indirectly bound excitons. However, strong interlayer Coulomb interactions are required to drive the superfluid phase transition which necessitates a thin barrier. We set  $\Delta_{sas} = 1 \mu\text{eV}$ , sufficiently small so that the lifetime of the indirectly bound exciton is long enough to observe condensation. Care must be taken when selecting the value of such a term; when we claim self-consistency in our simulations, we must have the changes in energy in successive iterations be smaller than the smallest energy scales in the system. Typically, the smallest energy scale in the system is  $\Delta_{sas}$ . While it is desirable to have the smallest possible splitting between the symmetric and anti-symmetric states, if the value selected is much smaller than the one we use in this work, self-consistency will require an intractably large number of iterations.

To summarize the procedure, we calculate the interlayer interaction  $\Delta$  in the system by calculating the single particle density matrix  $\rho$ . We insert  $\Delta$  back into the Hamiltonian  $\mathcal{H}_{BdG}$ . We iterate over these steps until every component of  $\Delta$  is equivalent to its value in the previous iteration, up to an error of  $\Delta_{sas}$ . When convergence is established, we calculate the magnitude of the order parameter using the expectation values of the density matrix in Eq. (16),

$$|m_{exc}| = \sqrt{(m_{exc}^x)^2 + (m_{exc}^y)^2} \tag{19}$$

Similarly, we may identify the phase of the order parameter dependent on the same expectation values of the density matrix [63],

$$\phi_{exc} = \tan^{-1} \left[ \frac{m_{exc}^y}{m_{exc}^x} \right]. \tag{20}$$

To understand the non-equilibrium evolution of the system, we first note that the transport properties are only dependent on the quasiparticle Hamiltonian and the chemical potentials of the leads. From this point, we may utilize another analogy to simplify the analysis. The excitonic superfluid state can equivalently be viewed in the language of a ‘‘pseudospin ferromagnet’’ [29, 64], which has been used extensively to understand interlayer tunneling conductance in the Quantum Hall Bilayers [27, 30, 32, 65, 66] mentioned in the introduction, and is likewise analogous to the double layer graphene system. The equivalence of the Hamiltonian to a ferromagnet means that the pseudospin magnetization dynamics must also satisfy the Landau-Lifshitz-Gilbert equation of magnetism. Because the pseudospin effective field is the only term in the Hamiltonian that does not conserve the  $\hat{z}$  component of the pseudospin, the quasiparticle wave function must satisfy [63, 67, 68]

$$\frac{\partial m_{exc}^z}{\partial t} = -\nabla \cdot \mathbf{j}^z + \frac{1}{\hbar}(\mathbf{m}_{exc} \times \Delta)_z, \tag{21}$$

where  $\mathbf{j}^z$  denotes  $\hat{z}$  component of the pseudospin current, i.e. it is the interlayer current if we return to the language of the double layer graphene superfluid. In steady state, it is clear that the time-dependent term must vanish so that the quasiparticle number currents in each layer reach constant values independent of time. Setting Eq. (21) to zero, we obtain

$$|m_{exc}| |\Delta| \sin(\phi_{exc} - \phi_{\Delta}) = \hbar \nabla \cdot \mathbf{j}^z, \tag{22}$$

where  $\phi_{\Delta}$  represents the planar orientation of  $\Delta$ . We may understand this equation by continuing our analogy between double layer systems and ferromagnetic metals. In ferromagnets, a large spin-splitting term lowers the energy of the quasiparticles whose spins are aligned with the magnetization relative to those other quasiparticles whose spins are

anti-aligned with the field. When a current flows in a ferromagnetic metal, the magnetization direction is altered resulting in the collective effect commonly referred to as the *spin-transfer torque*. The spin transfer torques can be thought of as the reaction counterparts of the torques which act on the quasiparticle spins that carry current through a non-collinear ferromagnet. The pseudospin orientation realigns as quasiparticles traverse the system; interlayer transport currents in this system can likewise be thought of as the *pseudospin torque effect* [63, 68].

While we have increased our insight into the interaction enhanced dynamics of the double layer graphene system, we must have an idea as to the strength of the interlayer interactions. We can take guidance from previous calculations that show the value of the order parameter is approximately one tenth the Fermi energy [37]. Our simulations show that this value of  $m_{exc}$  is achieved self-consistently when we set the interlayer coupling strength in Eq. (18) to  $U = 2.0$  eV. Although this is less than the unscreened mean-field interaction strength [61] ( $U = \frac{q^2}{\epsilon d} \approx 4.6$  eV), it is more plausible as it factors in damping effects due to screening [54]. Therefore, we use an interlayer interaction strength of  $U = 2.0$  eV for the remainder of this work.

#### 4.1 Quantum transport in ideal double layer graphene

We first study interlayer transport properties in ideal double layer graphene systems comprised of zigzag graphene nanoribbons. To obtain a more in-depth understanding of the interlayer transport in double layer graphene systems, we draw a comparison to Andreev reflection [69] in metal-superconductor interfaces to explain the non-equilibrium physics of the condensate. When an electron with energy less than the superconducting band gap is injected into a superconductor, the injected electron penetrates a certain distance, the coherence length, before it forms a Cooper pair that moves along the superconductor channel without dissipation. To conserve charge and momentum, a hole of opposite spin is retro-reflected into the normal lead, as shown in Fig. 6. For the analogous scenario in an exciton superfluid, an electron with energy less than the superfluid band gap injected into the system will form an exciton with a hole in the bottom monolayer, moving across the channel. To conserve charge and momentum, an electron is retro-reflected into the bottom left contact.

Put in the language of our double layer graphene system, an electron injected into the top left contact results in a dissipationless electron flow across the top layer and a electron flow in the opposite direction across the bottom layer. The configuration is known as the drag-counterflow geometry [61]. All non-equilibrium calculations described below are in this geometry, with the left and right contacts on the top monolayer set to magnitude of the counterflow

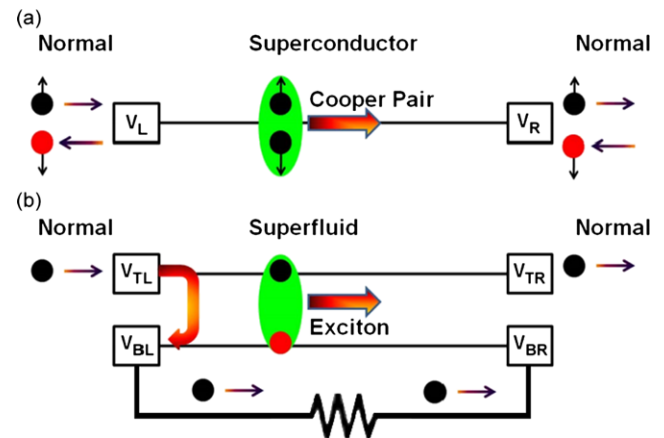


**Fig. 6** (a) Andreev reflection in a normal-superconductor-normal contact geometry yields an electron into the right lead and a hole out of the right lead to conserve momentum and total current. (b) Crossed Andreev reflection in the double layer graphene system yields a similar physics, with positive current in the top layer and negative current in the bottom layer in the drag-counterflow geometry ( $V_{TL} = -V_{TR} = V_{INT}$ ;  $V_{BL} = V_{BR} = 0$  V), which induces a current across an external load. Adapted from [70]

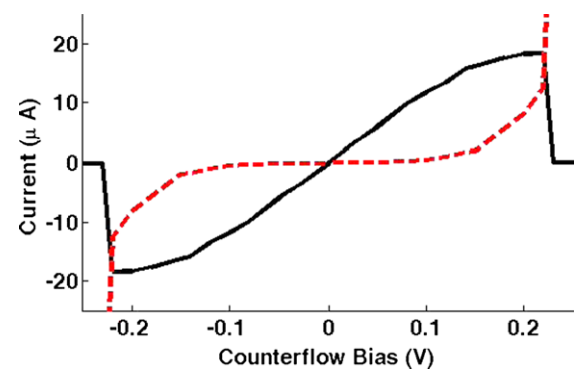


**Fig. 7** (Solid black) Interlayer and (dashed red) intralayer current plots for the ideal system as a function of counterflow bias. Adapted from [71] (Color figure online)

bias parameter ( $V_{TL} = -V_{TR} = V_{INT}$ ;  $V_{BL} = V_{BR} = 0$  V). The entire process results in a condensate current, due to the propagating exciton, and a quasiparticle current, caused by the injected and retro-reflected individual carriers. The quasiparticle current is only nonzero within the coherence length ( $L_c$ ), the maximum length an injected particle penetrates into the superfluid gap before the Andreev event occurs.

In Fig. 7, we present the observable interlayer and intralayer transport properties in the ideal case. Here we focus on the calculation and analysis of the critical tunneling current,  $I_c$  [19, 72, 73], which is the maximum current the system can sustain before phase coherence is lost. The critical current denotes the end of coherent interlayer transport, which is marked by a significant rise in the interlayer resistance for currents beyond the critical value, in agreement

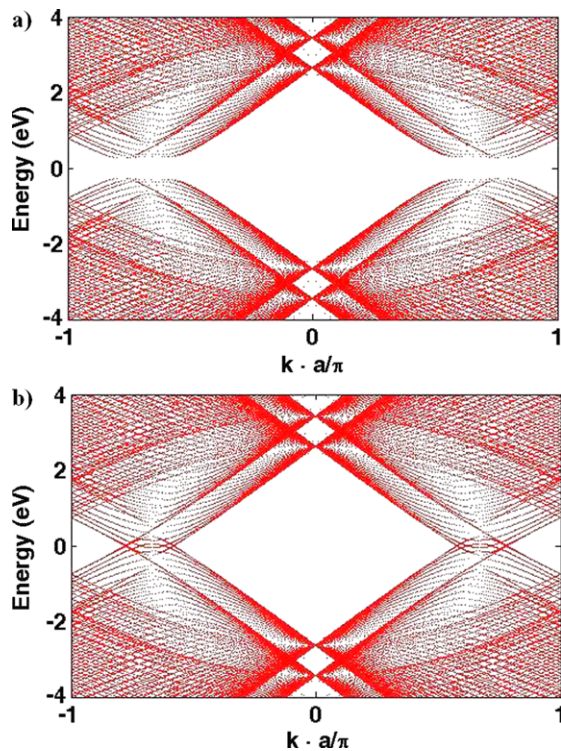


**Fig. 8** The dispersion relation for an ideal double layer graphene system in the transport direction (a) at a counterflow bias of  $V_{TL} = -V_{TR} = 0.05$  V which is below the critical current and (b) at a counterflow bias of  $V_{TL} = -V_{TR} = 0.23$  V which is above the critical current. Adapted from [71]

with previous predictions [74]. The currents are odd functions of the bias, reflecting the system’s ambipolar nature. At low bias, interlayer current is linear and interlayer conductance is constant, as injected carriers see the superfluid gap and trigger the Andreev event discussed above. Low-energy injected carriers are unable to pass through the superfluid gap, and intralayer current is negligible within this range. States above the superfluid band gap do begin to form at  $|E| \geq 0.14$  eV, as seen in the band structure in Fig. 8(a). Interlayer transmission quickly vanishes when higher energy states become accessible in the spectrum; transport along the monolayer dominates in these ranges. This is evidenced by the emergence of intralayer current and a drop in interlayer conductance beginning at a counterflow bias of 0.14 V.

Beyond a counterflow bias of  $0.22 \pm 0.01$  V, we pass the critical current of the system of  $I_c = \pm 18.4 \mu\text{A}$  and the superfluid can no longer adjust its phase to accommodate the interlayer current flow. Self-consistency is lost, and only single particle tunneling contributes to interlayer tunneling. The small magnitude of the resultant interlayer current, less than 1 pA for a bias of  $V_{TL} = -V_{TR} = 0.25$  V, is negligible compared to the many-body contribution to the interlayer current observed when the system obtains self-consistency. Additionally, past the critical current, no self-consistent solution to the steady-state transport characteristics is possible,

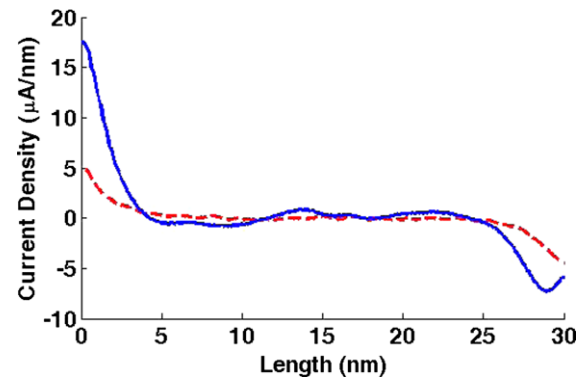


**Fig. 9** The interlayer quasiparticle current density along the transport direction in the ideal system averaged along the width of the system for counterflow biases of 0.05 V (red dashed line) and 0.20 V (blue solid line). The current density is only nonzero within the coherence length, which by inspection is approximately 5 nm. Quasiparticle current density is approximately odd about the center of the system at low bias, but symmetry is lost when a high contact bias limits carrier concentration on one side of the system. Adapted from [71] (Color figure online)

signaling that the dynamics of the system have become time-dependent [42, 68], and the steady state mean field equations no longer represent a valid description of the physics.

The phase transition that occurs beyond the critical current is shown in Fig. 8(b). Here we find that no superfluid gap remains in the dispersion relation of the ideal system. When no superfluid exists, each monolayer has a vanishing band gap and linear dispersion. As expected, the Dirac points occur in the normal phase at the  $K'$  and  $K$  points in the Brillouin zone with a Fermi energy of  $\pm 0.4$  eV. The band gap vanishes at biases which drive currents beyond the critical current. The closing of the band gap after the phase transition allows for more low energy states, causing a spike in intralayer current well beyond the range of interlayer transport in the superfluid phase.

The band structure in the transport direction of the system is derived [75] from a small portion of the converged Hamiltonian by assuming  $m_{exc}$  is periodic in the transport direction. This holds true only for the ideal system, where  $m_{exc}$  is smooth and consistent throughout the channel with a magnitude near 10 % of the Fermi energy and a phase of  $\pi/2$ . Randomly-placed impurities and vacancies, however, break the discrete translational invariance of the hexagonal lattice; the Hamiltonian is no longer periodic in the transport direction. We are thus unable to calculate the dispersion relations of disordered configurations.

Figure 9 plots the interlayer quasiparticle current densities along the transport direction averaged along the width of the system in an ideal system with a counterflow bias of 0.05 V and 0.20 V, just before the phase transition to a normal Fermi liquid state. Quasiparticle current tunneling, due to the aforementioned Andreev reflection process shown in Fig. 6, peaks at the contacts and evanescently decays into the channel, so that carriers which are involved in interlayer

transmission are only present a small distance into the channel, defined by this coherence length. Based on our simulations, at a Fermi energy of 0.4 eV in the top layer and  $-0.4$  eV in the bottom layer, we find the coherence length to be  $L_c \approx 5$  nm by inspection.

In order to solidify our understanding of the critical current in the ideal double layer graphene system, it is necessary to compare our numerical value with an analytic estimate of its value. In a system where coherence length is smaller than system length [74], the superfluid must satisfy an elliptic sine-Gordon equation,

$$\lambda^2 \nabla^2 \phi - \sin(\phi) = 0. \quad (23)$$

When this equation is solved in the static case, we obtain a relatively simple expression for the critical current in the ideal case,

$$I_c \sim \frac{eWm_{exc}}{\hbar L_c}. \quad (24)$$

For a system of width  $W = 10$  nm with a coherence length of  $L_c \approx 5$  nm and order parameter magnitude of  $|m_{exc}| \approx 0.04$  eV, the analytic critical current is roughly  $I_c^A \approx 19.5$   $\mu$ A. This is in good agreement with the critical current of  $I_c = \pm 18.4$   $\mu$ A calculated for an ideal system. The slight reduction in the critical current is expected from the electrostatically-based  $\Delta_z$  term that enters the self-consistent Hamiltonian separating the two nested Fermi surfaces and is not present in the analytic estimates.

Additionally, we find that interlayer quasiparticle current magnitude, shown in Fig. 9, is nearly equivalent at low bias but becomes very asymmetric near the critical transition point between superfluid behavior and Fermi liquid behavior. The Poisson equation in the counterflow bias configuration restricts the magnitude of the condensate order parameter because the negatively biased top right contact locally decreases the density of electrons able to pair into the condensate. Conversely, applying a bias across the hole-doped bottom layer will limit superfluid density and quasiparticle current near the left (positively biased) contact. The decreased density results in a smaller interlayer current density on one side of the system, as seen in the case with higher counterflow bias. The interlayer current is the current generated on the right side of the system; the side with limited exciton density is the transport bottleneck. A steady-state supercurrent is no longer possible when the disparity in condensate currents generated from each side of the system reaches a critical limit [61].

#### 4.2 Quantum transport in disordered double layer graphene

The complexity of the double layer graphene system makes it imperative to study the effects of lattice vacancies which

will inevitably arise during fabrication. Induced disorder in the system, evidenced by the marked reduction in mobility [76], can limit critical tunneling currents and may well be responsible for the lack of observation of a phase transition. Recent theoretical [77–83] and experimental [84, 85] studies have outlined the significant reductions in transport properties of single graphene layers when even small amounts of disorder are present in the system, but few currently consider the role of disorder in the case of double layer graphene superfluids other than to discuss the reduction in  $T_{KT}$  [86].

To better understand this interplay, we incorporate disorder into our model and investigate its effect on condensation and critical tunneling current. To model a vacancy, we modify the ideal Hamiltonian by setting all hopping to a missing atom to zero. This effectively blocks any interaction with the vacancy by setting the tight-binding overlap integral of the spatial  $p_z$  orbital states to zero [87]. We limit the degrees of freedom to only include disorder in one monolayer, randomly removing a fixed percentage of carbon atoms from the top monolayer while leaving the bottom monolayer unperturbed. Recent work suggests that, although vacancies in the graphene lattice may not be the dominant scattering mechanism, short-range scatterers can be modeled as vacancies which alter the localized density of states near the disorder [88, 89]. In fact, modeling a vacancy requires adding an on-site potential to the affected lattice point in the Hamiltonian to prevent hopping in the same way adding an on-site charged impurity potential does. Therefore, we conclude that the insertion of vacancies into the lattice is an appropriate model to study any such short-range disorder. Our simulations thus neglect the long-range effects caused by charged impurities and charge puddles in graphene, with characteristic lengths on the order of our system size [90, 91]. Long-range mitigating effects on superfluid transport involving the motion of vortex anti-vortex pairs [92] and unpaired vortices [93] have previously been studied in the context of Quantum Hall Bilayers, but are beyond the scope of this work.

In this section, we consider only disorder in the top layer while allowing the bottom layer to remain pristine. We focus on the scenario as it is the most likely experimental situation, in which the mobilities of individual layers end up disparate during fabrication [94]. We focus on the behavior of the disordered system in two distinct regions: (i) channel disorder, in the central section of the top layer past the coherence length and (ii) contact disorder, within the coherence length of the contacts. We show the main result of the lattice disorder analysis in Fig. 10, which plots the statistical variation in critical current as a function of vacancy concentration. Figure 10 shows two distinct trends for the two regions of top layer vacancies we consider. In the middle of the figure, at a vacancy concentration of 0 %, we plot the critical current we obtain for the ideal case. To the left of

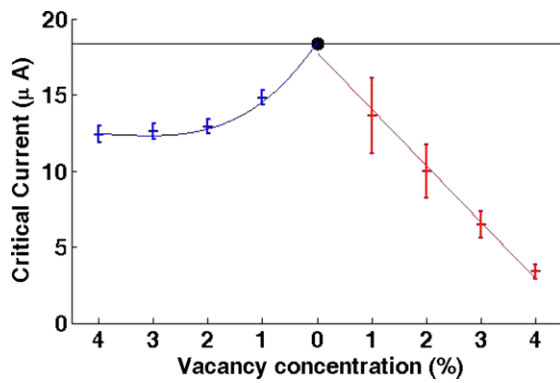


**Fig. 10** Statistical variation of  $I_c$  in the face of disorder. Channel disorder is shown in blue to the left of the ideal (0 %) case, depicted by a black circle. Contact disorder is shown in red to the right of the ideal case. Error bars show the variance in  $I_c$  over several runs. Self-consistency is lost in both cases for top layer vacancy concentrations larger than 4 %. The solid lines represent the expected relationship between ideal and disordered cases when using Eq. (24) with the values for superfluid density and effective width obtained from the disordered calculations, as described in Sect. 4.2. Adapted from [71] (Color figure online)

the ideal case, we plot the statistical variation in the critical current for channel disorder of increasing concentration. In this case, we find that the critical current decreases following an approximate square root dependence on the top layer vacancy concentrations. However, as the disorder only makes local perturbations to the system, reducing the local exciton concentrations, we find that the critical current is only degraded by 30 % of its original ideal value. Furthermore, we also notice that the mean of the statistical distribution of critical currents associated with various top layer vacancy distributions varies only by approximately 5 % even as the concentration of vacancies is increased.

As we move away from the ideal case towards the right hand side of Fig. 10, we plot the statistical change of the critical current associated with contact disorder. Here we see a stark contrast in behavior, with critical current depending linearly on the concentration of vacancies. We also see that there are very large variations in the location of the critical current as we shift the locations of the top layer vacancies. No steady-state superfluid density can be found when more than 4 % vacancies are included in one monolayer in both disorder cases, suggesting systems with large amounts of disorder prevent the realization of the superfluid. Inter-layer currents become several orders of magnitude smaller as the majority of the current injected into the uncondensed system only flows across the graphene layers.

To better understand the reduction in interlayer current as channel disorder is increased, we examine the magnitude of the order parameter,  $|m_{exc}|$ . In Fig. 11, we plot the magnitude of the order parameter for a random vacancy concentration of 1 %. In this situation, we find that the order parameter magnitude does not remain constant over the entire system

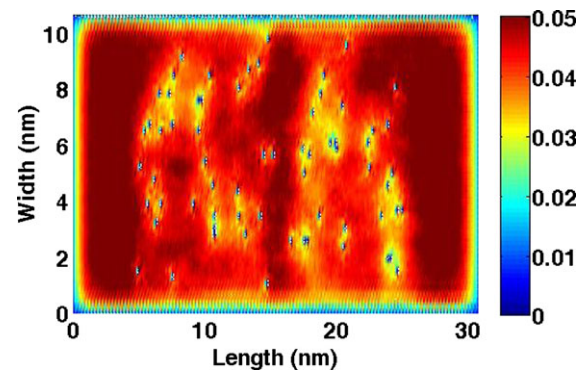


**Fig. 11**  $|m_{exc}|$  for a system with 1 % channel vacancies. The condensate is very close to that of the ideal case, with a drop in magnitude only occurring locally near disorder. As expected,  $|m_{exc}| \approx 0.1 E_F$  away from disorder. Adapted from [71]

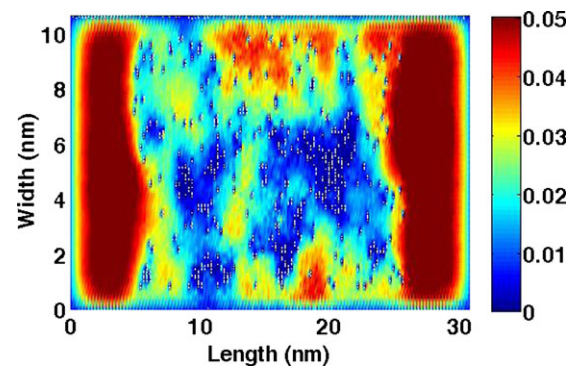


**Fig. 12**  $|m_{exc}|$  for a system with 4 % channel vacancies. Magnitude clearly drops nonlinearly with the increase in disorder, but quasiparticle current is still able to form near the contacts. Adapted from [71]

at a value of 10 %  $E_F$ , as was the case in the ideal system. We see that vacancies locally destroy the condensate [54] and reduce  $|m_{exc}|$  at surrounding points up to a distance of 0.5 nm away, or three to four nearest neighbors from the vacancies. However, no long range effect is seen when vacancies are isolated from one another by more than approximately 2 nm. At this particular vacancy concentration, we find that  $m_{exc}$  is reduced by 40 % over an appreciable area of our system as a result of these vacancies.

This situation is to be contrasted with Fig. 12 where we plot  $|m_{exc}|$  for a channel vacancy concentration of 4 %. In this case, significant areas clearly emerge where concentrated disorder has long range effects on superfluid density. These areas of high vacancy concentrations in Fig. 12 give rise to values for  $|m_{exc}|$  that are less than 20 % the ideal value over significant areas of the system. Superfluid magnitude remains at its ideal level near the contacts, sufficiently quarantined from the vacancies.

The root cause of the sub-linear degradation seen  $I_c$  as we increase the top layer vacancy concentration can be explained by examining the local density of states (LDOS) [95] in the monolayer. Vacancies induce a LDOS

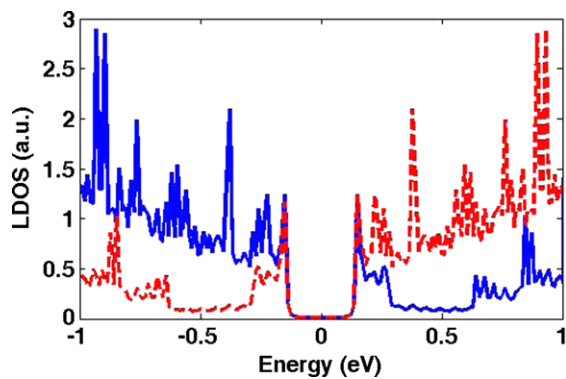


**Fig. 13** Low-energy local density of states in the ideal system. The solid blue (dashed red) line represents the top (bottom) layer. No localized states exist below a magnitude of 0.14 eV for the superfluid. Adapted from [71] (Color figure online)

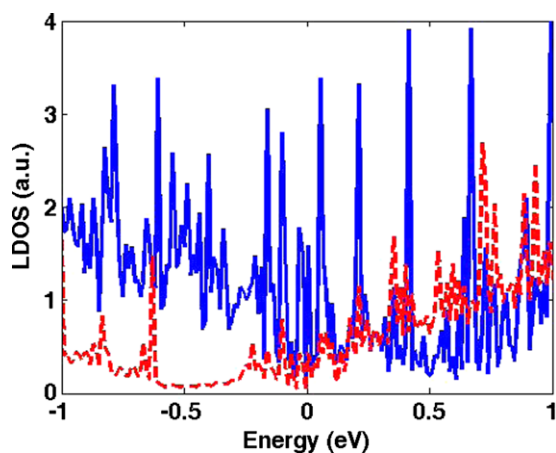


**Fig. 14** Low-energy local density of states in a system with 4 % channel vacancies. The solid blue (dashed red) line represents the top (bottom) layer. Low energy states due to the vacancies introduces a weak but apparent LDOS in the ideal bottom layer as well, due to the thinness of the spacer dielectric. Adapted from [71] (Color figure online)

similar to the case of an impurity [96, 97] in graphene layers. In Figs. 13 and 14 we plot the LDOS for the ideal case and for the case of 4 % top layer vacancy concentration as an average along the disordered area of each monolayer. We plot an average to show the magnitude of uncoupled states that form not only at vacancies, but at neighboring locations and in the ideal bottom layer as a result of electrostatics. We clearly see a stark contrast in the low-energy LDOS in the superfluid phase when vacancies are introduced. The LDOS closely resembles those of monolayer graphene at higher energies, with peaks at  $E = E_F \pm t$ , where  $t$  is the nearest neighbor hopping energy of Eq. (11) [89]. The ideal top and bottom monolayers exhibit perfectly antisymmetric densities of states so that equivalent carrier concentrations arise in the oppositely gated top and bottom monolayers. We find that no states exist in the superfluid gap in the ideal double

layer, as one would expect for a condensate in which all of the quasiparticles participate.

The biased top and bottom gates, necessary to generate the sufficient carrier concentrations, cause the undesirable occupation of the mid-gap states of Fig. 14 up to the Fermi energy, which act to scatter excitons traversing through the layer and change the interlayer phase relationship. Localized states also arise, to a lesser degree, in the bottom layer from the Coulomb attraction of the filled mid-gap states in the top layer through the thin spacer dielectric. This effects a change in the  $\Delta_y$  term in Eq. (16). As a result, when the decreased interlayer phase relationship is input into the calculation of  $m_{exc}$  in Eq. (19),  $|m_{exc}|$  drops by 30 % from its ideal value of 41 meV at 4 % top layer vacancy concentration. The reduced interlayer phase component decreases  $|m_{exc}|$  in a rough square root correlation. Recalling from Eq. (24) that critical current is directly proportional to  $|m_{exc}|$ , we plot on the left hand side of Fig. 10 the ratio of the channel-disordered  $|m_{exc}|$  to the value of  $|m_{exc}|$  in the clean limit to show the nature of the degradation of  $I_c$  is due to the decrease in superfluid density, finding excellent agreement between the two values. The square root dependence is not exact and saturates at higher disorder concentrations because  $m_{exc}$  is not affected near the contact regions and is allowed to remain at its ideal value, as seen in Fig. 12. The average coupling strength does not change appreciably between disorder configurations, resulting in critical current approximations with small deviations relative to the contact disordered scenario.

While we have shown the double layer graphene system is fairly robust to vacancies deep in the channel, this is not the case for contact disorder in the top layer, where interlayer current is extremely sensitive to the specific location and amount of disorder. When contact disorder increases,  $|m_{exc}|$  decays in a similar fashion to what is shown in Figs. 11 and 12, but is localized near the contacts on either side of the channel. Quasiparticle current density is proportional to the magnitude of the order parameter, causing it to drop appreciably. Groups of vacancies cause a nonlinear, long-range drop in superfluid density. Top layer vacancies closest to the contact, where quasiparticle tunneling magnitude is largest, cause the biggest detriment to the magnitude of interlayer current. Despite the vacancies reducing the space in which quasiparticles may be injected without scattering, we still find that the condensate is able to form. Little randomized bunching occurs in the 1 % case, as the disorder is too sparse to create significantly different scenarios. Interlayer current remains rather robust, roughly 30 % smaller than ideal. The random nature of the placement, however, causes a high variance in interlayer current in this scenario unlike the channel-disordered scenario.

Significant amounts of clustering occur as we move to higher contact vacancy concentrations and the available

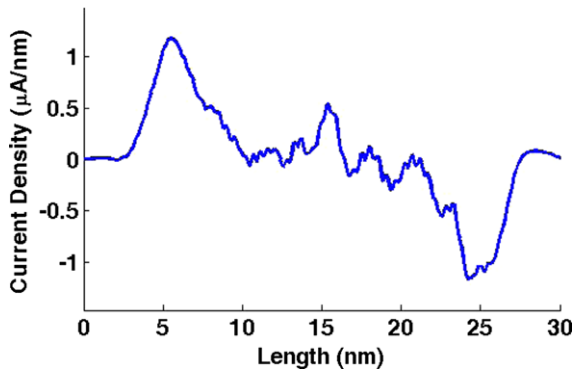


**Fig. 15** Quasiparticle current density for a system with 4 % contact disorder with a counterflow bias of 0.04 V, just before the phase transition. No condensate exists near the contacts, so the largely degraded quasiparticle tunneling that does occur only happens beyond the disorder. Adapted from [71]

space for quasiparticles may be injected is greatly reduced. This results in a very different transport relationship compared to the case of channel disorder. Carriers injected into the system see a significant reduction in the area in which quasiparticle tunneling can occur near the contact, significantly reducing conductivity. As we know that there is a linear dependence on the width of the system in Eq. (24), this gives a very simple explanation for the physics of the linear decrease in the critical current observed in Fig. 10. This information allows us to conclude that graphene with vacancies within the coherence length effectively reduces the width over which quasiparticle tunneling occurs, and causes a linear decay in  $I_c$  with respect to contact disorder strength until the condensate vanishes. We add a linear line of best fit to the right hand side of Fig. 10, and by inspection find that a 1 % increase in contact vacancy concentration mitigates the effective width of the superfluid channel by roughly 20 %.

In Fig. 15, we show that the average interlayer quasiparticle current density qualitatively shifts when top layer vacancies are included within the coherence length of the top layer contacts. Equivalent disorder concentrations generate disparate condensate currents on each side because vacancies are randomly configured to be more closely lumped near one contact than the other. Whereas superfluid excitons are able to permeate disorder as long as the condensate exists, an increasing proportion of bare electrons and holes cannot penetrate the contact disorder to reach the condensate. The critical bias at which the phase transition occurs decreases as disorder increases because of the discrepancy in condensate current from each contact. The on-site potential is greater at vacancies near the contacts due to  $V_{TR}$  and  $V_{TL}$ . The LDOS is more quickly occupied, and further accelerates the phase transition. As a result, critical current roughly drops linearly, down to a degradation of 80 % for a vacancy concentration 4 %, before self-consistency is lost.

### 4.3 Phonon-limited quantum transport in double layer graphene

If double layer graphene is capable of achieving superfluidity at elevated temperatures, such as room temperature, then to understand the quantum transport characteristics requires us to examine the interplay between the constituent quasiparticles and relevant phonon modes to determine the role of electron-phonon interactions on the superfluid [98]. We introduce the quasiparticle-phonon interaction by adding self-energy scattering terms to the double layer graphene Hamiltonian within the self-consistent Born approximation. In the low phonon wave vector limit ( $\mathbf{q} \rightarrow 0$ ), the self-energy in-scattering and out-scattering components are completely diagonal and simplify to [99]

$$\begin{aligned} \Sigma^{in/out}(\mathbf{r}, E) = & K_{ac} G^{n/p}(\mathbf{r}, E) \\ & + K_{op}(\omega_0)(n_0 + 1)G^{n/p}(\mathbf{r}, E \pm \hbar\omega_0) \\ & + K_{op}(\omega_0)n_0 G^{n/p}(\mathbf{r}, E \mp \hbar\omega_0), \end{aligned} \quad (25)$$

where  $G^{n/p}(\mathbf{r}, E)$  are the electron- and hole-correlated Green functions of the system and  $n_0 \approx \frac{k_B T}{\hbar\omega_0}$  is the temperature-dependent phonon occupation number for vanishing phonon wave vector.  $K_{ac}$  and  $K_{op}(\omega_0)$  denote the elastic acoustic and inelastic optical phonon coupling constants. They can be written as

$$\begin{aligned} K_{ac} = & \frac{D_{ac}^2 k_B T}{\rho v_{ac}^2 a_{cc}^2}, \\ K_{op}(\omega_0) = & \frac{D_{op}^2 \hbar}{2\rho\omega_0 a_{cc}^2}, \end{aligned} \quad (26)$$

where  $\rho$  denotes the gate voltage-tuned quasiparticle density of each layer,  $a_{cc} = 0.142$  nm is the carbon-carbon bond length, and we set  $T = 300$  K for room temperature consideration. For graphene, the acoustic and optical phonon deformation potentials are  $D_{ac} = 19$  eV and  $D_{op} = 10^9$  eV/cm, and first optical phonon branch is located at  $\hbar\omega_0 = 164.6$  meV [100, 101]. We set the velocity of sound in the lattice to  $v_{ac} = 2 \times 10^6$  cm/s [102]. We iterate the coupled set of equations until both  $m_{exc}$  and  $G^{n/p}(\mathbf{r}, E)$  converge to self-consistent values below the single particle tunneling energy,  $\Delta_{sas}$ .

We plot the current-voltage characteristic for a large and small quasiparticle density in Fig. 16. We immediately see that phonons in the graphene lattice have very little effect on interlayer current for high quasiparticle density. At lower quasiparticle density, however, phonons can play a significant role in limiting the superfluid performance. At  $V_G = 0.20$  V, the critical current drops by 66 % from the ballistic value of  $I_c \approx 10.0$   $\mu$ A.

We plot the critical current over a wide range of gate voltage configurations for both the ballistic and phonon-limited

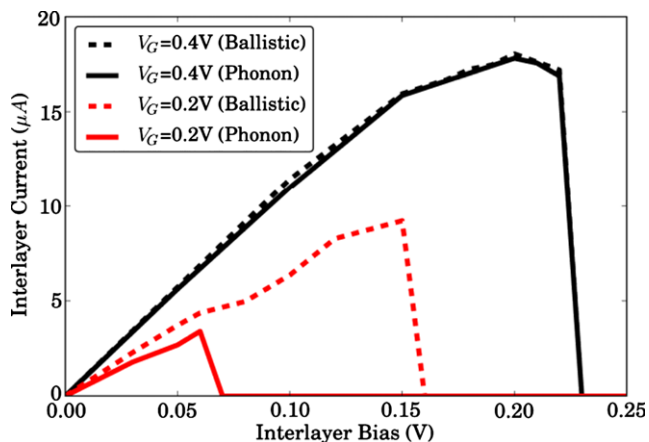


**Fig. 16** Calculated  $I$ - $V$  characteristic comparing (dotted lines) ballistic and (solid lines) phonon-limited cases for two gate voltages, (black)  $V_G = 0.4$  V and (red)  $V_G = 0.2$  V. Adapted from [103] (Color figure online)

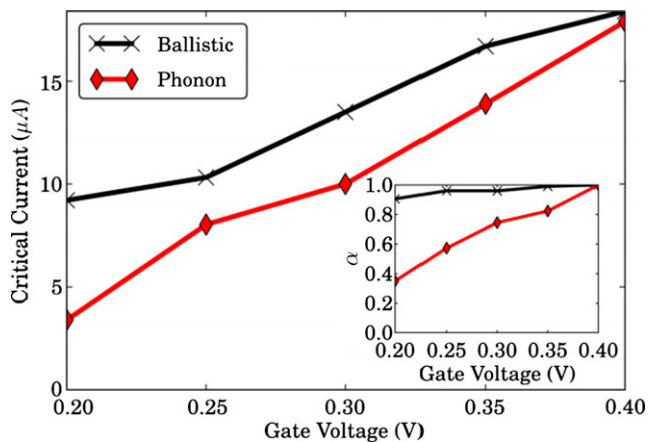


**Fig. 17** Critical current  $I_c$  dependence on gate voltage  $V_G$  for the (black) ballistic case and (red) when phonons are introduced. *Inset*: The average value of superfluid density, with and without phonon interactions, normalized to the value of  $|m_{exc}|$  calculated at  $V_G = 0.4$  V:  $\alpha \equiv |m_{exc}|/|m_{exc}|(V_G = 0.4 \text{ V})$ . Adapted from [103] (Color figure online)

cases in Fig. 17. Gate voltages below 0.20 V are expected to be well outside the predicted spinless room-temperature superfluid regime and are neglected in the study. In the ballistic case, we see a linear decay in  $I_c$  due to the linear dependence on  $E_F$  and  $k_F$ , as expected from Eq. (24). However, when we examine the phonon-limited transport, we observe that the critical current decays at an accelerated rate away from  $V_G = 0.4$  V, signifying that other factors are limiting the interlayer transport properties.

To explain the non-linear drop in phonon-limited interlayer current, we investigate the dependence of the magnitude of the order parameter on gate voltage in the inset of Fig. 17.  $|m_{exc}|$  remains virtually unchanged as  $V_G$  decreases in the ballistic case, with a small drop at very low gate voltage due to confinement effects. When phonon in-

teractions are added, however, the order parameter decreases dramatically. Phonon scattering serves to energetically separate the excitons, prematurely breaking interlayer coherence once the scattering energy exceeds the exciton binding energy within the condensate. This yields a drop in  $|m_{exc}|$  and, therefore, an enhanced degradation in  $I_c$  relative to the ballistic case.

## 5 Summary and conclusions

In conclusion, we have examined both the equilibrium and non-equilibrium properties of high-temperature superfluids in double layer graphene systems. Through the use of Path Integral Quantum Monte Carlo techniques, we have shown that the Kosterlitz-Thouless transition temperature for indirectly bound excitonic superfluids in spinless bilayer systems lies well above room temperature. Furthermore, we find that even above the transition temperature the system is comprised of preformed excitons which have not undergone a phase transition. When we add additional degrees of fermionic freedom, we find a weaker interlayer interaction strength which serves to reduce the transition temperature. Nevertheless, we find that its effect is mitigated as intralayer correlations suppress the additional screening, yielding a higher transition temperature incommensurate with predictions based on large- $N$  analysis.

To understand the quantum transport properties of the double layer graphene system, we perform self-consistent transport calculations within the non-equilibrium Green function formalism. We calculate a critical interlayer current and find that it is in good agreement with analytical estimates in the ideal case obtained by solving the Sine-Gordon equation. We find that disorder outside of the coherence length in the graphene channels produces only a small effect on interlayer transport. However, vacancies within the coherence length significantly obstruct transport by effectively reducing the width over which interlayer transport occurs, necessitating high-quality contacts for optimal superfluid transport. Although the system remains fairly robust to lattice disorder, significant vacancy concentrations of 5 % or higher prevents the steady-state formation of the condensate.

When considering the role of quasiparticle-phonon interactions in the system, we find that the system is robust to phonon scattering if the quasiparticle density is sufficiently large. However, if the top and bottom gate voltages yield smaller carrier concentrations, critical current can decay significantly due to a large degradation in the many-body order parameter. It is thus important to populate the monolayers with a very large and equivalent concentration of electrons and holes in order to make it robust to phonon interactions, so that it can persist at ambient temperature.

**Acknowledgements** The authors would like to thank J.-J. Su, A.H. MacDonald, S. Datta, N. Neophytou and G. Liang for insightful discussions on the mean-field approach and NEGF formalism and J. Shumway for contributions and discussions related to the PIMC formalism.

## References

1. Snoke, D.: *Science* **298**, 1368 (2002)
2. Balili, R.B., Hartwell, V., Snoke, D., Pfeiffer, L., West, K.: *Science* **316**, 1007 (2007)
3. Christopoulos, S., Hörger von Högersthal, G.B., Grundy, A.J.D., Lagoudakis, P.G., Kavokin, A.V., Baumberg, J.J., Christmann, G., Butté, R., Feltin, E., Carlin, J.F., Grandjean, N.: *Phys. Rev. Lett.* **98**, 126405 (2007)
4. Butov, L.V., Gossard, A.C., Chemla, D.S.: *Nature* **418**, 751 (2002)
5. Baranov, M.A., Mar'enko, M.S., Rychkov, V.S., Shlyapnikov, G.V.: *Phys. Rev. A* **66**, 013606 (2002)
6. Neely, T.W., Samson, E.C., Bradley, A.S., Davis, M.J., Anderson, B.P.: *Phys. Rev. Lett.* **104**, 160401 (2010). doi:[10.1103/PhysRevLett.104.160401](https://doi.org/10.1103/PhysRevLett.104.160401)
7. Hadzibabic, Z., Krüger, P., Cheneau, M., Battelier, B., Dalibard, J.: *Nature* **441**, 1118 (2006)
8. Potter, A.C., Berg, E., Wang, D.W., Halperin, B.I., Demler, E.: *Phys. Rev. Lett.* **105**, 220406 (2010)
9. Wang, D.W.: *Phys. Rev. Lett.* **98**, 060403 (2007)
10. Huang, X., Dietsche, W., Hauser, M., von Klitzing, K.: *Phys. Rev. Lett.* **109**, 156802 (2012). doi:[10.1103/PhysRevLett.109.156802](https://doi.org/10.1103/PhysRevLett.109.156802)
11. Tutuc, E., Shayegan, M., Huse, D.A.: *Phys. Rev. Lett.* **93**, 036802 (2004)
12. Wiersma, R.D., Lok, J.G.S., Kraus, S., Dietsche, W., von Klitzing, K., Schuh, D., Bichler, M., Tranitz, H.P., Wegscheider, W.: *Phys. Rev. Lett.* **93**, 266805 (2004)
13. Kellogg, M., Eisenstein, J.P., Pfeiffer, L.N., West, K.W.: *Phys. Rev. Lett.* **93**, 036801 (2004)
14. Kellogg, M., Spielman, I.B., Eisenstein, J.P., Pfeiffer, L.N., West, K.W.: *Phys. Rev. Lett.* **88**, 126804 (2002)
15. Wiersma, R.D., Lok, J.G.S., Kraus, S., von Klitzing, W.D.K., Schuh, D., Bichler, M., Tranitz, H.P., Wegscheider, W.: *Physica E, Low-Dimens. Syst. Nanostruct.* **34**, 16 (2006)
16. Pillarisetty, R., Noh, H., DePootere, E.P., Tsui, D.C., Shayegan, M.: *Physica E, Low-Dimens. Syst. Nanostruct.* **22**, 300 (2004)
17. Plochocka, P., Schneider, J.M., Maude, D.K., Potemski, M., Rappaport, M., Umansky, V., Bar-Joseph, I., Groshaus, J.G., Gallais, Y., Pinczuk, A.: *Phys. Rev. Lett.* **102**, 126806 (2009)
18. Yoon, Y., Tiemann, L., Schmult, S., Dietsche, W., von Klitzing, K., Wegscheider, W.: *Phys. Rev. Lett.* **104**, 116802 (2010)
19. Tiemann, L., Dietsche, W., Hauser, M., von Klitzing, K.: *New J. Phys.* **10**, 045018 (2008)
20. Tiemann, L., Lok, J.G.S., Dietsche, W., von Klitzing, K., Muraki, K., Schuh, D., Wegscheider, W.: *Phys. Rev. B* **77**, 033306 (2008)
21. Tiemann, L., Lok, J.G.S., Dietsche, W., von Klitzing, K., Muraki, K., Schuh, D., Wegscheider, W.: *Physica E, Low-Dimens. Syst. Nanostruct.* **40**, 1034 (2008)
22. Fertig, H.A.: *Phys. Rev. B* **40**, 1087 (1989)
23. Wen, X.G., Zee, A.: *Phys. Rev. Lett.* **69**, 1811 (1992)
24. Moon, K., Mori, H., Yang, K., Girvin, S.M., MacDonald, A.H., Zheng, L., Yoshioka, D., Zhang, S.C.: *Phys. Rev. B* **51**, 5138 (1995)
25. Halperin, B.I., Lee, P.A., Read, N.: *Phys. Rev. B* **47**, 7312 (1993)
26. Fil, D.V., Shevchenko, S.I.: *Low Temp. Phys.* **33**, 780 (2007)
27. Park, K., DasSarma, S.: *Phys. Rev. B* **74**, 035338 (2006)
28. Cote, R., Boisvert, D.B., Bourassa, J., Boissonneault, M., Fertig, H.A.: *Phys. Rev. B* **76**, 125320 (2007)
29. Stern, A., Girvin, S.M., MacDonald, A.H., Ma, N.: *Phys. Rev. Lett.* **86**, 1829 (2001)
30. Balents, L., Radzihovsky, L.: *Phys. Rev. Lett.* **86**, 1825 (2001). doi:[10.1103/PhysRevLett.86.1825](https://doi.org/10.1103/PhysRevLett.86.1825)
31. Murthy, G., Sachdev, S.: *Phys. Rev. Lett.* **101**, 226801 (2008)
32. Fogler, M.M., Wilczek, F.: *Phys. Rev. Lett.* **86**, 1833 (2001). doi:[10.1103/PhysRevLett.86.1833](https://doi.org/10.1103/PhysRevLett.86.1833)
33. He, S., DasSarma, S., Xie, X.C.: *Phys. Rev. B* **47**, 4394 (1993)
34. MacDonald, A.H.: *Physica B* **289**, 129 (2001)
35. Jungwirth, T., MacDonald, A.H.: *Phys. Rev. Lett.* **87**, 216801 (2001)
36. Zhang, C.H., Joglekar, Y.N.: *Phys. Rev. B* **77**, 233405 (2008)
37. Min, H.K., Bistritzer, R., Su, J.J., MacDonald, A.H.: *Phys. Rev. B* **78**, 121401 (2008)
38. Gilbert, M., Shumway, J.: *J. Comput. Electron.* **8**, 51 (2009). doi:[10.1007/s10825-009-0286-y](https://doi.org/10.1007/s10825-009-0286-y)
39. Neto, A.H.C., Guinea, F., Peres, N.M.R., Novoselov, K.S., Geim, A.K.: *Rev. Mod. Phys.* **81**, 109 (2009)
40. Banerjee, S., Register, L., Tutuc, E., Reddy, D., MacDonald, A.: *IEEE Electron Device Lett.* **30**(2), 158 (2009). doi:[10.1109/LED.2008.2009362](https://doi.org/10.1109/LED.2008.2009362)
41. Gilbert, M.J.: *IEEE Trans. Electron Devices* **57**, 3059 (2010)
42. Gilbert, M.J.: *Phys. Rev. B* **82**, 165408 (2010). doi:[10.1103/PhysRevB.82.165408](https://doi.org/10.1103/PhysRevB.82.165408)
43. Ceperley, D.M.: *Phys. Rev. Lett.* **69**, 331 (1992). doi:[10.1103/PhysRevLett.69.331](https://doi.org/10.1103/PhysRevLett.69.331)
44. Pierleoni, C., Ceperley, D.M., Bernu, B., Magro, W.R.: *Phys. Rev. Lett.* **73**, 2145 (1994). doi:[10.1103/PhysRevLett.73.2145](https://doi.org/10.1103/PhysRevLett.73.2145)
45. Feynman, R.P.: *Statistical Mechanics*. Addison-Wesley, Reading (1972)
46. Feynman, R.P.: *Phys. Rev.* **91**, 1291 (1953). doi:[10.1103/PhysRev.91.1291](https://doi.org/10.1103/PhysRev.91.1291)
47. Reynolds, P.J., Ceperley, D.M., Alder, B.J., Lester, W.A.: *J. Chem. Phys.* **77**(11), 5593 (1982). <http://link.aip.org/link/?JCP/77/5593/1>. doi:[10.1063/1.443766](https://doi.org/10.1063/1.443766)
48. Shumway, J., Ceperley, D.M.: *Solid State Commun.* **134**, 19–22 (2005)
49. Akkineni, V.K., Ceperley, D.M., Trivedi, N.: *Phys. Rev. B* **76**, 165116 (2007). doi:[10.1103/PhysRevB.76.165116](https://doi.org/10.1103/PhysRevB.76.165116)
50. Zhu, X., Littlewood, P.B., Hybertsen, M.S., Rice, T.M.: *Phys. Rev. Lett.* **74**, 1633 (1995). doi:[10.1103/PhysRevLett.74.1633](https://doi.org/10.1103/PhysRevLett.74.1633)
51. De Palo, S., Rapisarda, F., Senatore, G.: *Phys. Rev. Lett.* **88**, 206401 (2002). doi:[10.1103/PhysRevLett.88.206401](https://doi.org/10.1103/PhysRevLett.88.206401)
52. Bouabca, T., Amor, N.B., Maynau, D., Caffarel, M.: *J. Chem. Phys.* **130**, 114107 (2009)
53. Avouris, P., Chen, Z., Perebeinos, V.: *Nat. Nanotechnol.* **2**, 605 (2007)
54. Kharitonov, M.Y., Efetov, K.B.: *Phys. Rev. B* **78**, 241401R (2008)
55. Shumway, J., Gilbert, M.J.: *Phys. Rev. B* **85**, 033103 (2012). doi:[10.1103/PhysRevB.85.033103](https://doi.org/10.1103/PhysRevB.85.033103)
56. Ceperley, D.M.: *Rev. Mod. Phys.* **67**, 279 (1995). doi:[10.1103/RevModPhys.67.279](https://doi.org/10.1103/RevModPhys.67.279)
57. Datta, S.: *Superlattices Microstruct.* **28**, 253 (2000)
58. Datta, S.: *Quantum Transport: Atom to Transistor*. Cambridge University Press, Cambridge (2005)
59. Liang, G., Neophytou, N., Lundstrom, M.S., Nikonov, D.E.: *Nano Lett.* **8**(7), 1819 (2008). PMID:18558785. doi:[10.1021/nl080255r](https://doi.org/10.1021/nl080255r)
60. Guo, J.: *Purdue University* (2005)
61. Su, J.J., MacDonald, A.H.: *Nat. Phys.* **4**, 799 (2008)
62. Johnson, D.D.: *Phys. Rev. B* **38**, 12807 (1988)

63. Gilbert, M.J.: Phys. Rev. B **82**(16), 165408 (2010). doi:[10.1103/PhysRevB.82.165408](https://doi.org/10.1103/PhysRevB.82.165408)
64. Rossi, E., Heinonen, O.G., MacDonald, A.H.: Phys. Rev. B **72**, 174412 (2005)
65. Joglekar, Y.N., MacDonald, A.H.: Phys. Rev. Lett. **87**, 196802 (2001). doi:[10.1103/PhysRevLett.87.196802](https://doi.org/10.1103/PhysRevLett.87.196802)
66. Nunez, A.S., MacDonald, A.H.: Solid State Commun. **139**(1), 31 (2006). <http://www.sciencedirect.com/science/article/pii/S0038109806003772>. doi:[10.1016/j.ssc.2006.05.004](https://doi.org/10.1016/j.ssc.2006.05.004)
67. Su, J.J., MacDonald, A.H.: Phys. Rev. B **81**(18), 184523 (2010). doi:[10.1103/PhysRevB.81.184523](https://doi.org/10.1103/PhysRevB.81.184523)
68. Kim, Y., MacDonald, A.H., Gilbert, M.J.: Phys. Rev. B **85**, 165424 (2012)
69. Andreev, A.F.: Sov. Phys. JETP **19**, 1228 (1964)
70. Gilbert, M.J.: IEEE Trans. Electron Devices **57**, 3059 (2010)
71. Dellabetta, B., Gilbert, M.J.: J. Phys. Condens. Matter **23**(34), 345302 (2011). <http://stacks.iop.org/0953-8984/23/i=34/a=345302>
72. Tiemann, L., Yoon, Y., Dietsche, W., von Klitzing, K., Wegscheider, W.: Phys. Rev. B **80**, 165120 (2009)
73. Su, J.J., MacDonald, A.H.: Phys. Rev. B **81**(18), 184523 (2010). doi:[10.1103/PhysRevB.81.184523](https://doi.org/10.1103/PhysRevB.81.184523)
74. Su, J.J., MacDonald, A.H.: Phys. Rev. B **81**, 184523 (2010)
75. Luisier, M., Schenk, A., Fichtner, W., Klimeck, G.: Phys. Rev. B **74**(20), 205323 (2006). doi:[10.1103/PhysRevB.74.205323](https://doi.org/10.1103/PhysRevB.74.205323)
76. Kim, S., Jo, I., Nah, J., Yao, Z., Banerjee, S.K., Tutuc, E.: Phys. Rev. B **83**, 161401 (2011)
77. Ihnatsenka, S., Kirczenow, G.: Phys. Rev. B **80**, 201407R (2009)
78. Adam, S., Brouwer, P.W., DasSarma, S.: Phys. Rev. B **79**, 201404R (2009)
79. Cresti, A., Roche, S.: Phys. Rev. B **79**, 233404 (2009)
80. Basu, D., Gilbert, M.J., Register, L.F., Banerjee, S.K., MacDonald, A.H.: Appl. Phys. Lett. **92**, 042114 (2008)
81. Martin, I., Blanter, Y.M.: Phys. Rev. B **79**, 235132 (2009)
82. Klos, J.W., Shylau, A.A., Zozoulenko, I.V., Xu, H., Heinzl, T.: Phys. Rev. B **80**, 245432 (2009)
83. Yoon, Y., Guo, J.: Appl. Phys. Lett. **91**, 073103 (2007)
84. Gallagher, P., Todd, K., Goldhaber-Gordon, D.: Phys. Rev. B **81**, 115409 (2010)
85. Lin, Y.M., Perebeinos, V., Chen, Z., Avouris, P.: Phys. Rev. B **78**, 161409R (2008)
86. Bistritzer, R., MacDonald, A.H.: Phys. Rev. Lett. **101**, 256406 (2008)
87. Anantram, M.P., Govindan, T.R.: Phys. Rev. B **58**(8), 4882 (1998). doi:[10.1103/PhysRevB.58.4882](https://doi.org/10.1103/PhysRevB.58.4882)
88. Ferreira, A., Viana-Gomes, J., Nilsson, J., Mucciolo, E.R., Peres, N.M.R., Castro Neto, A.H.: Phys. Rev. B **83**(16), 165402 (2011). doi:[10.1103/PhysRevB.83.165402](https://doi.org/10.1103/PhysRevB.83.165402)
89. Yuan, S., De Raedt, H., Katsnelson, M.I.: Phys. Rev. B **82**(11), 115448 (2010). doi:[10.1103/PhysRevB.82.115448](https://doi.org/10.1103/PhysRevB.82.115448)
90. Deshpande, A., Bao, W., Zhao, Z., Lau, C.N., LeRoy, B.J.: Phys. Rev. B **83**(15), 155409 (2011). doi:[10.1103/PhysRevB.83.155409](https://doi.org/10.1103/PhysRevB.83.155409)
91. Das Sarma, S., Adam, S., Hwang, E.H., Rossi, E.: Rev. Mod. Phys. **83**, 407 (2011). doi:[10.1103/RevModPhys.83.407](https://doi.org/10.1103/RevModPhys.83.407)
92. Fertig, H.A., Murthy, G.: Phys. Rev. Lett. **95**, 156802 (2005)
93. Huse, D.A.: Phys. Rev. B **72**, 064514 (2005)
94. Kim, S., Jo, I., Nah, J., Yao, Z., Banerjee, S.K., Tutuc, E.: Phys. Rev. B **83**, 161401 (2011). doi:[10.1103/PhysRevB.83.161401](https://doi.org/10.1103/PhysRevB.83.161401)
95. Neophytou, N., Ahmed, S., Klimeck, G.: J. Comput. Electron. **6**, 317 (2007). doi:[10.1007/s10825-006-0116-4](https://doi.org/10.1007/s10825-006-0116-4)
96. Pereira, V.M., Guinea, F., Lopes dos Santos, J.M.B., Peres, N.M.R., Castro Neto, A.H.: Phys. Rev. Lett. **96**(3), 036801 (2006). doi:[10.1103/PhysRevLett.96.036801](https://doi.org/10.1103/PhysRevLett.96.036801)
97. Bácsı, A., Virosztek, A.: Phys. Rev. B **82**(19), 193405 (2010). doi:[10.1103/PhysRevB.82.193405](https://doi.org/10.1103/PhysRevB.82.193405)
98. Akturk, A., Goldsman, N.: J. Appl. Phys. **103**(5), 053702 (2008). doi:[10.1063/1.2890147](https://doi.org/10.1063/1.2890147)
99. Nikonov, D., Pal, H., Bourianoff, G.: (2009). <http://nanohub.org/resources/7772>
100. Borysenko, K.M., Mullen, J.T., Barry, E.A., Paul, S., Semenov, Y.G., Zavada, J.M., Nardelli, M.B., Kim, K.W.: Phys. Rev. B **81**, 121412 (2010). doi:[10.1103/PhysRevB.81.121412](https://doi.org/10.1103/PhysRevB.81.121412)
101. Yoon, Y., Nikonov, D.E., Salahuddin, S.: Appl. Phys. Lett. **98**(20), 203503 (2011). <http://link.aip.org/link/?APL/98/203503/1>. doi:[10.1063/1.3589365](https://doi.org/10.1063/1.3589365)
102. Hwang, E.H., Das Sarma, S.: Phys. Rev. B **77**, 115449 (2008). doi:[10.1103/PhysRevB.77.115449](https://doi.org/10.1103/PhysRevB.77.115449)
103. Estrada, Z.J., Dellabetta, B., Ravaioli, U., Gilbert, M.J.: IEEE Electron Device Lett. **33**(10), 1465 (2012). doi:[10.1109/LED.2012.2207701](https://doi.org/10.1109/LED.2012.2207701)